JOURNAL OF PROPULSION AND POWER
Vol. 20, No. 6, November–December 2004

Mathematical Modeling of the Development of Anomalous Processes in High-Loading-Density Solid Propulsion Systems

Alexey M. Lipanov,* Alexander N. Lukin,† and Ali V. Aliev‡
Russian Academy of Sciences, 426067, Udmurtia Republic, Russia

One of the important directions for research in the area of high-loading-density solid propulsion systems (SPS) is the investigation of the technologies for optimal organization of the intrachamber processes during the ignition-transient period of operation, with aim of reducing the shock and vibrational loads on the rocket and its systems. A numerical study of anomalous physico-chemical processes was carried out. Calculation results show that anomalous modes of ignition (which are accompanied by intense shock waves in the high-loading-density SPS combustion chamber) are extremely dangerous. The calculations demonstrate that the anomalous physicochemical processes in the SPS can be prevented. The appropriate technology and an ignition system design for prevention of anomalous ignition of the solid propellant charge were developed.

Nomenclature

A, b = mass concentrations of combustion products formed at the solid propellant burning surface and flowing into the front head-end clearance through its opened boundary
C = speed of sound
C_C = specific heat capacity of the solid propellant
C_{f0} = friction coefficient
Co = Courant number, stability coefficient
C_p = constant-pressure specific heat capacity of the combustion products
C_v = constant-volume specific heat capacity of the combustion products
d = diameter of clearance
D_{PC} = diameter of the solid propellant charge
E = energy of the combustion products mixture (sum of the combustion product internal and kinetic energy)
E_a = reaction activation energy
F = area or front end-face cavity (clearance) cross-sectional area
F_{CC} = solid propellant rocket motor combustion chamber throat area
$F_{\mathrm{op}}^{\mathrm{IS}}$ = solid propellant rocket motor ignition system total perforation opening area
H = propellant enthalpy
K_b, K_{def} = coefficient of proportionality, determined experimentally
k = adiabatic exponent (specific heat ratio)
k_0 = preexponent
L = length of clearance
L_{IS} = length of the ignition system
L_{PC} = length of the solid propellant rocket motor charge
M = Mach number
P = combustion product mixture pressure
P_b = combustion product pressure value in the boot area
P_D = engine pressure sealing diaphragm destruction pressure value
Per = clearance lateral surface perimeter
P_{sup} = support pressure, 0.981×10^5 Pa
P_0 = environmental pressure
P_* = boot break-off pressure value
Q = reaction heat effect
q_s = heat flow value on the propellant surface
q_U = value of radiative heat flow into the combustion products
R = gas constant or clearance curvature radius
Re = Reynolds criterion
R_0 = universal gas constant
r = distance from the symmetry axis
S_{PC} = solid propellant burning surface area
T = temperature
T_{ig} = critical temperature
t = process time
t_* = solid propellant surface ignition delay time (surface, located in the reopened end-face cavity)
U = longitudinal component of the combustion product flow velocity
u_c = solid propellant linear burning rate
u_1 = individual burning rate in the degree combustion law (temperature-dependent constant)
V = lateral component of the combustion product flow velocity
W^{IS} = solid propellant rocket motor ignition system chamber internal volume value
W_0 = volume value of the reopened cavity at $P = P_0$
α = heat exchange coefficient
γ_c = relative mass concentration of the c phase in the combustion product mixture
Δ = clearance between engine case head-end internal surface and charge end-face surface
Δt = time step in the finite difference scheme
$\Delta\xi$ = step along the solid propellant rocket motor curvilinear zone longitudinal direction at finite difference solution of the equations
ε = combustion product blackness coefficient
$\varepsilon_{\mathrm{eb}}$ = coefficient of erosive burning
ε_s = propellant surface blackness coefficient
η = density of the volumetric incident radiation or diametrical coordinate of the solid propellant rocket motor curvilinear zone (solid propellant rocket motor front end-face clearance)

Received 30 November 1997; accepted for publication 8 March 2004.

*Professor, Academician, Institute of Applied Mechanics, Ural Branch.
†Senior Scientist, Institute of Applied Mechanics, Ural Branch, and Professor–Advisor, Shaanxi Research Institute of Applied Physics–Chemistry, X'ian, Shaanxi Province, People's Republic of China.
‡Professor, Institute of Applied Mechanics, Ural Branch; currently Professor, Izhevsk State Technical University, Izhevsk 426069.

η_{EC} = coordinate of the engine case internal surface (boundary coordinate)
η_{SP} = coordinate of the solid propellant external surface (boundary coordinate)
θ = peripheral coordinate
λ = heat conductivity coefficient
μ = combustion product dynamic viscosity coefficient
ν_c = exponent in the degree combustion law (pressure exponent)
ξ = longitudinal coordinate in the solid propellant rocket motor curvilinear zone (coordinate along the solid propellant rocket motor front head-end clearance axis)
$\bar{\xi}$ = ξ relative value, ξ/L
ρ = density or combustion product mixture density
Σ_a, Σ_t = coefficients of radiation and combustion product interaction (function of the combustion product properties)
σ = Stefan–Boltzman constant
τ = friction stress
ω_{IS} = mass of the pelletized solid propellant, placed in the ignition system cavity

Subscripts and Superscripts

b = boundary
calc = obtained computationally
CP = combustion products
c = condensed (solid) phase (solid propellant)
EC = internal surface of the solid propellant rocket motor head end
exp = obtained experimentally
ig = moment of propellant ignition
IS = ignition system
LB = left (opened) clearance boundary
RB = right (nonflowing) clearance boundary
SP = external surface of solid propellant rocket motor charge
s = propellant suface
st = stationary values
0 = initial conditions
1 = solid propellant combustion products
2 = combustion products entering the clearance through the opened boundary
3 = gas originally filling the clearance

Introduction

THE evolutionary history of solid propellants reflects to some extent the history of the investigation of unstable combustion and methods for its prevention and restriction. The general tendency in the development of modern large-sized solid propellant rocket motors (SPRM) is characterized by increased propellant mass (propellant loading density ≥ 0.95) and operation loads. Improvement of the characteristics of modern high-loading-density SPRM and reduction in the cost and difficulty involved in their manufacture depend largely on improved understanding of the anomalous physics–chemical processes that can arise during operation.

The most important area of study for the improvement of high-loading-density SPRM characteristics is the investigation and creation of technologies to optimize the intrachamber processes of the SPRM ignition-transient period of operation to reduce impact and vibrational loads on the SPRM. It is necessary to provide short propellant charge ignition delay times and ignition-transient periods without increasing the pressure level in the combustion chamber and thermal loads on the solid propellant charge and the engine combustion chamber structural elements.

The main peculiarity of such propulsion systems is that the case-bonded charge with internal channel has a partially nonfastening and unarmored end-face surface. Under these conditions, the end-face combustion surface can represent up to 50% or even more of the whole combustion surface. The charge end face is usually fastened to the engine head end by use of a boot (sealing ring). Figure 1 shows a typical structural diagram of this type of SPRM, where 1 indicates the lid, 2 the engine casing, 3 the case-bonded solid propellant charge, 4 the fastening layer connecting propellant charge with load-carrying SPRM case, 5 the pyrotechnic ignition system (IS), 6 the split control nozzle, 7 the autonomous solid propellant engines for roll channel control, and 8 the actuators. The engine case has a cocoon-type design and is manufactured from organic plastic materials.

The other peculiarity of this class of SPRM is that under normal conditions the clearance between the engine case head-end internal surface and the charge end-face surface $\Delta \leq 0.001$ m. As the chamber is filled by the high-temperature combustion products (CP) coming from the IS and from the ignited part of the propellant, there are simultaneous elastic deformations of the propellant charge and the engine case. Under such conditions, the thickness of the nonflowing clearance between the SPRM case head-end internal surface and the charge end-face clearance can increase 20–100 times at the operating pressures in the combustion chamber (5–10 MPa). In Fig. 2, the dependence of the front end-face clearance cross-sectional area on the longitudinal coordinate is shown for various time intervals: 1) $t = 0$ s, 2) 0.036 s, 3) 0.048 s, and 4) 0.060 s. Here the coordinate $\xi = 0$ corresponds to the boundary between the end-face cavity and the engine front volume. The coordinate system is shown in Fig. 3.

The investigation of flame propagation processes in narrow, flowing-type channels and in solid propellant cracks was undertaken for cases when the convective combustion mode was

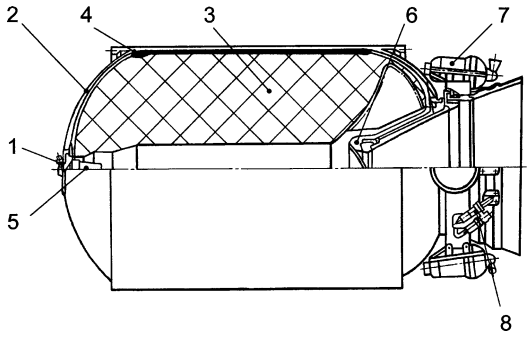

Fig. 1 High-loading-density sustainer SPRM design of the intercontinental ballistic rocket third stage: 1, lid; 2, fiber-glass engine case; 3, case-bonded solid propellant charge; 4, fastening layer connecting propellant charge to load-carrying SPRM case; 5, pyrotechnic ignition system; 6, split control nozzle; 7, autonomous solid propellant engines for roll channel control; and 8, actuators.

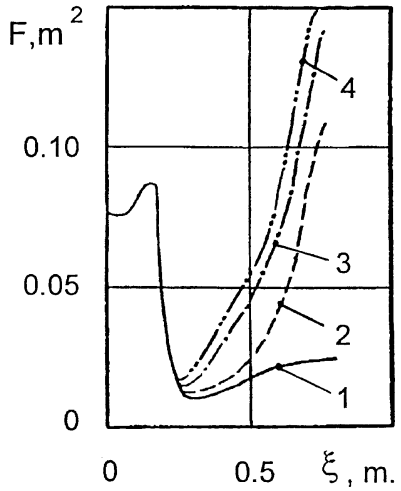

Fig. 2 Front-end-face clearance cross-sectional area in the vicinity of the engine front bottom vs longitudinal coordinate for various time intervals: 1, $t = 0$ s, 2, $t = 0.036$ s, 3, $t = 0.048$ s; and 4, $t = 0.060$ s.

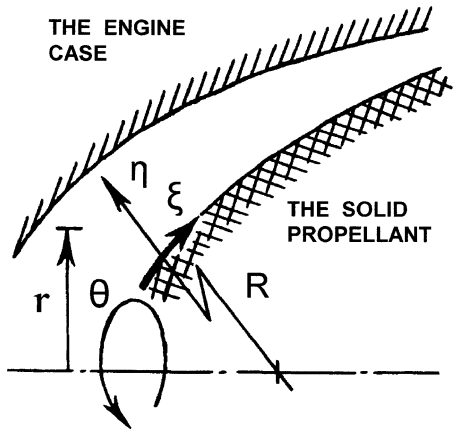

Fig. 3 Computational area of the SPRM curvilinear zone (SPRM front-end-face clearance).

realized and was presented in previous papers.[1,2] Investigations of the flame propagation processes along the propellant surface in the narrow, nonflowing, and deformable channel have also been presented elsewhere.[3,4] The present research considers the case when a new cavity is opened on the boundary between the narrow nonflowing end-face clearance and the boot. This occurs when the boot, which fastens together the solid propellant charge endface and the engine head end, breaks off from the engine case and from the charge. This newly opened cavity also represents a nonflowing channel. The appearance of the new cavity causes the development of anomalous physicochemical processes. Special attention is given to the question of radiative heat transmission during the analysis of propellant heat-up because the convective heat flows have small values. Under these conditions, the radiative heat flow lengthways is additionally taken into account on the narrow clearance.

Development of Anomalous Processes

In a number of cases, the earlier-mentioned peculiarities of the SPRM can cause the increased tendency of the SPRM initial-stage operation to various kinds of unpredictable behaviors. These unpredictable behaviors include deviations from the working parameters of the separate units and elements of the SPRM and may be the result of design errors, or failure to predict technological process modes or aging of the materials, in the design of both the SPRM and the charge.

The intraballistic parameters in the ignition-transient period of high-loading-density SPRM operation are determined in many respects by the physicochemical processes in the pyrotechnic IS and subsequent heat effect of the IS charge CP on the motor main charge. In the situation considered here, the cause of an anomalous mode of ignition and combustion in the SPRM can result in unpredictable action from the pyrotechnic IS. Such unpredictable (and uncalculated) effects result in nonuniformity of the working processes during propellant charge ignition. Traditional IS design schemes provide CP to the high-loading-density SPS charge simultaneously in all directions. In the course of filling the intrachamber volume with CP coming from the IS and from the already ignited part of the charge, simultaneous elastic deformations of the propellant charge and the organic plastic engine case may occur. However, the elongated nonflowing end-face clearance has no time to be expanded to the necessary size. When this occurs, in the most crucial period of operation in this class of SPRM, anomalous physicochemical processes capable of significantly affecting engine operation can be initiated.

The most probable sequence of anomalous-mode ignition development is as follows. The end-face clearance, being a poorly heated stagnation zone, will reduce the supply of heat available for ignition of the charge front-end face. In the absence of carefully distributed CP flows from the IS, it may also result in much greater irregularity of the heat supply to the charge. It will lead to an increase in the front-end face ignition time delay and to the nonuniformity of all charge ignition processes. Furthermore, in the early stages of ignition, the CP flowing into and out of the IS, and from the ignited charge sections, will compress the gas initially placed in the end-face clearance. Compression waves will begin to propagate into the depths of the end-face clearance and, typically, form an intensive shock wave. The latter, on reaching the area of interface of the engine head end with the boot and the charge end-face, is reflected by simultaneously built-up pressure. Then, propagation of a reflected shock wave begins, and the initial gas, which is contiguous to the area of interface of the engine head end with the boot and the charge end face, will be compressed to high pressure.

In the area of the interface of the end-face clearance cavity with the boot, which fastens the charge end face with the engine head end, this process can give rise to strong local dynamic loads, causing the boot to break off either from the engine case or from the charge or from both. Numerical analysis shows that, for a clearance of $\Delta = 0.001$ m, the maximum pressure in the end-face clearance cavity will exceed 13 times the pressure level, corresponding to a clearance of $\Delta = 0.1$ m. The boot breaking off from the engine case is accompanied by the opening of a new cavity, into which the high-temperature CP begins to flow. At this point, the anomalous process development begins on a new qualitative level. Such anomalous behaviors can have large-scale effects on the SPRM intrachamber processes.

The further development of nonstationary physicochemical processes can endanger the normal functioning of the SPRM. If the surface from which the boot breaks off is large, the intraballistic process in the engine chamber can develop in the following way: Over time the CP pressure near the point where the boot breaks off can decrease, and a rarefaction wave will be propagated in the SPRM chamber. In case of a strong rarefaction wave, the propellant charge may be completely or temporarily extinguished, or the propellant charge may transition to unsteady burning modes (SPRM chuffing).[5] Propagation of the compression wave along the cavity formed where the boot breaks off can result in ignition of the opened propellant surface and can create dangerously large pressures in the vicinity of the upper boundary of the cavity. This, in turn, can result in the destruction of the propellant charge.

Also, in traditional IS design schemes, it is necessary to increase the IS mass flow rate characteristics and the heat flow from the CP to intensify the solid propellant charge ignition process and reduce the ignition-transient period time. In this situation, however, the increased thermal effects on the solid propellant charge induce charge burn out and an extreme pressure rise (pressure peak) in the engine combustion chamber. Intensive, non stationary axial pressure differentials will arise between the various charge channel cross sections. As a result, before the nozzle plug opening, high nonestimated vibrational and impact loads arise and act on the solid propellant charge and the SPRM case. These loads may cause both break off of the charge from the engine case and destruction of the charge and, thus, result in loss of functionality of the SPRM, the onboard control system, and the rocket.

Attempts to improve this situation without changing traditional IS design schemes, by reduction of the IS charge mass and the standard IS flow rate characteristics, and also by reduction of the opening pressure of the SPRM nozzle plug, results in reduction of the reliability of the SPRM charge front-end face clearance surface ignition, especially, under low-temperature conditions.

Assumptions

When a mathematical model was constructed of anomalous physicochemical processes in the SPRM end-face clearance, after boot break off, the following assumptions were made: The cold gas originally occupying the clearance cavity, the hot CP coming through the opened boundary into the computational domain from the IS, and the solid propellant CP, all form a chemically nonreacting mixture, the flow of which is nonstationary and follows the laws of ideal gas flow. In the CP mixture, condensed particles can be present, at rates and temperatures that coincide with the corresponding parameters of the gas. The heat flows from the CP to the propellant charge and the engine case are determined by using the criteria relations. Boot break off occurs instantaneously. The friction losses

and the heat transfer from the CP mixture into the propellant and the material of the end-face clearance walls are taken into account by introducing source terms into the momentum and energy equations. The gas mixture is transparent. The solid phase thermophysical coefficients do not depend on space and time. Last, the solid propellant located in the narrow and nonflowing end-face clearances is ignited and heated by the hot CP, which flows through the opened boundary into the domain to be computed.

Mathematical Model

Let us consider two-dimensional differential gasdynamics equations for the CP flow in the SPRM curvilinear zone (the SPRM front-end face clearance) (Fig. 1). A diagram of the SPRM curvilinear zone (the SPRM front-end face clearance) is shown in Fig. 3. Here r and R are the distance from the symmetry axis and the curvature radius of the clearance, respectively. The orthogonal coordinate system is designated by ξ, η, and θ. Because the end-face clearance value is small, it is reasonable to assume that the variation in gasdynamics parameters in the direction along the clearance thickness is negligible. Moreover, we believe that the curvature of the calculated area can be ignored, that is, $R_1^{\max}/R \ll 1$, where $R_1 = r_{\mathrm{EC}} - r_{\mathrm{SP}}$. In accordance with these assumptions, all of the gasdynamics parameters are averaged across η,

$$\frac{\partial \eta_{\mathrm{EC}}}{\partial \xi}, \qquad \frac{\partial \eta_{\mathrm{SP}}}{\partial \xi}, \qquad \frac{1}{\mathrm{r}} \cdot \frac{\partial \eta_{\mathrm{EC}}}{\partial \theta}, \qquad \frac{1}{\mathrm{r}} \cdot \frac{\partial \eta_{\mathrm{SP}}}{\partial \theta} \ll 1$$

$$\frac{\partial \eta_{\mathrm{EC}}}{\partial t} = \frac{\partial \eta_{\mathrm{SP}}}{\partial t} \approx 0$$

For flow of the CP mixture along the clearance, in the orthogonal coordinate system (ξ, θ), this equation has the following form:

$$\frac{\partial}{\partial t} A + \frac{\partial}{\partial \xi} B + \frac{1}{R_2} \cdot \frac{\partial}{\partial \theta} C + D = M \tag{1}$$

where

$$A = \begin{bmatrix} \rho \cdot R_3 \\ \rho \cdot a \cdot R_3 \\ \rho \cdot b \cdot R_3 \\ \rho \cdot U \cdot R_3 \\ \rho \cdot V \cdot R_3 \\ \rho \cdot E \cdot R_3 \end{bmatrix} \qquad B = \begin{bmatrix} \rho \cdot U \cdot R_3 \\ \rho \cdot a \cdot U \cdot R_3 \\ \rho \cdot b \cdot U \cdot R_3 \\ \rho \cdot U^2 \cdot R_3 \\ \rho \cdot U \cdot V \cdot R_3 \\ \rho \cdot U \cdot \left[E + \dfrac{P}{\rho} \right] \cdot R_3 \end{bmatrix}$$

$$R_2 = 0.5 \cdot (r_{\mathrm{EC}} + r_{\mathrm{SP}}), \qquad R_3 = R_1 \cdot R_2$$

$$C = \begin{bmatrix} \rho \cdot V \cdot R_3 \\ \rho \cdot a \cdot V \cdot R_3 \\ \rho \cdot b \cdot V \cdot R_3 \\ \rho \cdot U \cdot V \cdot R_3 \\ \rho \cdot V^2 \cdot R_3 \\ \rho \cdot V \cdot \left[E + \dfrac{P}{\rho} \right] \cdot R_3 \end{bmatrix}, \qquad D = \begin{bmatrix} 0 \\ 0 \\ 0 \\ R_3 \cdot \dfrac{\partial}{\partial \xi} P \\ R_1 \cdot \dfrac{\partial}{\partial \theta} P \\ 0 \end{bmatrix}$$

$$M = \begin{bmatrix} \rho_c \cdot u_c \cdot r_{\mathrm{SP}} \\ \rho_c \cdot u_c \cdot r_{\mathrm{SP}} \\ 0 \\ -r_{\mathrm{SP}} \cdot \tau_S \\ 0 \\ \rho_c \cdot u_c \cdot r_{\mathrm{SP}} \cdot H + (q_U - q_S) \cdot r_{\mathrm{SP}} \end{bmatrix}$$

Moreover, because the geometry of the calculated area does not depend on the peripheral coordinate θ in the design considered here, we assume that partial derivatives on the peripheral coordinate θ are equal to zero and also that $V = 0$. Multiplying the left-hand and right-hand parts of Eq. (1) by the $2 \cdot \pi$ value, and taking into account that $(2 \cdot \pi \cdot R_1 \cdot R_2) = F$, and $(2 \cdot \pi \cdot r_{\mathrm{SP}}) = \mathrm{Per}$, we obtain

$$\frac{\partial}{\partial t}(F \cdot \rho) + \frac{\partial}{\partial \xi}(F \cdot \rho \cdot U) = \rho_c \cdot u_c \cdot \mathrm{Per}, \qquad t > 0 \tag{2}$$

$$\frac{\partial}{\partial t}(F \cdot \rho \cdot a) + \frac{\partial}{\partial \xi}(F \cdot \rho \cdot a \cdot U) = \rho_c \cdot u_c \cdot \mathrm{Per}, \qquad t > 0 \tag{3}$$

$$\frac{\partial}{\partial t}(F \cdot \rho \cdot b) + \frac{\partial}{\partial \xi}(F \cdot \rho \cdot b \cdot U) = 0, \qquad t > 0 \tag{4}$$

$$\frac{\partial}{\partial t}(F \cdot \rho \cdot U) + \frac{\partial}{\partial \xi}(F \cdot \rho \cdot U^2) + F \cdot \frac{\partial P}{\partial \xi} = -\mathrm{Per} \cdot \tau_S \tag{5}$$

$$\frac{\partial}{\partial t}(F \cdot \rho \cdot E) + \frac{\partial}{\partial \xi}\left(F \cdot \rho \cdot U \cdot \left[E + \frac{P}{\rho} \right] \right) = \rho_c \cdot u_c \cdot \mathrm{Per} \cdot H + (q_U - q_s) \cdot \mathrm{Per} \tag{6}$$

$$C_p = C_{p1} \cdot a + C_{p2} \cdot b + C_{p3} \cdot (1 - a - b) \tag{7}$$

$$a = \frac{\rho_1}{\rho} \tag{8}$$

$$b = \frac{\rho_2}{\rho} \tag{9}$$

$$C_v = C_{v1} \cdot a + C_{v2} \cdot b + C_{v3} \cdot (1 - a - b) \tag{10}$$

$$R = C_p - C_v \tag{11}$$

$$k = \frac{C_p}{C_v} \tag{12}$$

$$P = \rho \cdot (k - 1) \cdot (E - 0.5 \cdot U^2) \tag{13}$$

The experimental results show that the engine case deformation is determined by the CP pressure level in the SPRM combustion chamber (the pressure on the opened boundary of the end-face clearance, through which the hot CP flow into area to be computed). During engine operation, the thickness of the clearances between the charge end face and the engine head end can change under linear law, depending on the pressure level in the central charge channel. The end-face clearance cross-sectional area is determined by the following empirical relation:

$$F(\xi, t) = F(\xi, 0) \cdot [1 + K_{\mathrm{def}} \cdot (P_{\mathrm{LB}}/P_0 - 1)] \tag{14}$$

The volume of the newly opened cavity is simulated by the following relation:

$$W = W_0 \cdot [1 + K_b \cdot (P_b/P_{\mathrm{sup}})] \tag{15}$$

For the gasdynamic solution of the open (left) boundary, the following additional conditions are set. For the CP subsonic flow into the end-face clearance through the open boundary, the conditions are $P_{\mathrm{LB}} = P(t)$ and $T_{\mathrm{LB}} = T(t)$, for the CP subsonic flow out of the end-face clearance, the sufficient condition is $P_{\mathrm{LB}} = P(t)$. In case of sonic (or supersonic) CP efflux from the end-face clearance, additional conditions on the parameters on the open boundary are not required. On the right-hand (nonflowing) boundary, the inflow conditions[4] are accepted.

In the CP mixture energy equation, the radiative heat flow value q_U into the CP is determined by solving the following equations[6]:

$$\frac{\mathrm{d}}{3} \cdot \frac{\partial}{\partial \xi} \frac{1}{\Sigma_t} \frac{\partial \eta}{\partial \xi} = \sigma \cdot T^4 \cdot \frac{\varepsilon \cdot \varepsilon_s}{\varepsilon + \varepsilon_s - \varepsilon \cdot \varepsilon_s} + q_U$$

$$q_U = \Sigma_a \cdot \mathrm{d} \cdot (\eta - 4 \cdot \sigma \cdot T^4) \tag{16}$$

The boundary-value problem for the incident radiation density η is decided at the next boundary conditions:

$$\eta_{\mathrm{LB}} = 4 \cdot \sigma \cdot T_{\mathrm{LB}}^4, \qquad \frac{\partial \eta_{\mathrm{RB}}}{\partial \xi} = 0 \tag{17}$$

The propellant heating is determined from the following correlations:

$$\frac{\mathrm{d}}{\mathrm{d}t}(T_s - T_0)^2 = \frac{2}{C_C \cdot \lambda_C \cdot \rho_C} \cdot q_s^2$$

$$q_s = \alpha \cdot (T - T_s) + \sigma \cdot \left(T^4 - T_s^4\right) \cdot \frac{\varepsilon \cdot \varepsilon_s}{\varepsilon + \varepsilon_s - \varepsilon \cdot \varepsilon_s}$$

$$\alpha = 0.332 \cdot \frac{\lambda}{\mathrm{d}} \cdot \left(\frac{\rho \cdot U \cdot \mathrm{d}}{\mu}\right)^{0.5} \cdot \left(1 + \frac{\xi}{\mathrm{d}}\right)^{-0.5} \tag{18}$$

These correlations are obtained under the hypothesis that the propellant surface heated by convective and radiative heat transfer, the convective heat flow realized in the laminar mode, and the heated propellant layer all have temperature profiles of an exponential form. Equation (18) is integrated in each section of the end-face clearance up to the moment when the propellant ignition conditions are satisfied for that section,[7]

$$T_s \geq T_{\mathrm{ig}}$$

$$q_s \leq \rho_c \cdot \lambda_c \cdot T_s \cdot k_0 \cdot Q \cdot [(R \cdot T_s)/E_a] \cdot \exp[-E_a/(R \cdot T_s)] \tag{19}$$

In system (19), the $\top_{\mathrm{ig}}$ value is determined empirically, and the q_s value corresponds to the sum of the convective and the radiative heat flow components.

The integral dependencies suggested by Bobrishev are used to account for the possible erosive effect of the solid propellant burning (see Ref. 8). The basis of this procedure is the solution of the asymptotic equations of heat conduction and diffusion in the gas phase of the burning propellant. The distinctive feature of Bobrishev's model consists in that threshold (critical) values of the velocity of the CP flow, below which there is no erosive burning, are not required for each specific solid propellant.

According to this procedure, the erosive coefficient $\varepsilon_{\mathrm{eb}}$, is determined on the basis of the following relationships:

$$\varepsilon_{\mathrm{eb}} = \sqrt{0.5 + \sqrt{0.25 + [\kappa_0 \cdot \eta_T \cdot \mathrm{th}(-\eta_T/30)]^2}} \tag{20}$$

$$\kappa_0 = 0.39 \tag{21}$$

$$\eta_T = (0.675 \cdot \eta_s + 2.1) \cdot \mathrm{th}(\eta_s/3.25) \tag{22}$$

$$\eta_s = 2.2 \cdot \rho \cdot |U| \cdot \sqrt{C_{\mathrm{f0}}/2} \cdot \left[1/\rho_c \cdot u_c^{\mathrm{st}}\right] \tag{23}$$

$$\sqrt{C_{\mathrm{f0}}/2} = \left[5.5 + 2.5 \cdot \ell_n\left(Re \cdot \sqrt{C_{\mathrm{f0}}/2}\right)\right]^{-1} \tag{24}$$

The last equation is solved iteratively. For the first approximation it is believed that $C_{f0} = 0.04$.

All of the flow rate characteristics are determined in accordance with the dependencies given in Refs. 9 and 10.

Numerical Algorithm

The set of Eqs. (2–24) is substantially nonlinear, and therefore, we shall use numerical methods for the processes development analysis. System (2–13), describing the gasdynamic processes, represents a set of differential equations with partial derivatives of a hyperbolic type. For this study we shall employ the large-particle method developed by Davydov.[11–13]

The large-particle method is a method for computing compressible flows of a continuous medium. The method is based on splitting the original differential equations in accordance with the physical processes they represent. It can be used to solve systems of evolution equations. The procedure may establish the existence of steady-state solutions. The large-particle method is a development of Harlow's particles in cell method. The method is widely used to investigate aerodynamic flows, diffraction problems, transonic flows, and the interaction of radiation and matter, among other things.

The solution process is divided into three chronological stages, each of which consists of three steps: an Eulerian, a Lagrangian, and a third final step. One first considers the variations in the internal state of a subsystem, a large particle (Eulerian step), and then the motion of this subsystem with the interior state of the subsystem left unchanged (Lagrangian and third final steps). In the Eulerian step, the domain of integration is covered by a stationary (Eulerian) difference grid of arbitrary form. In this step of the calculation, only quantities relating to the cell as a whole are varied, and the fluid is assumed to be momentarily constrained. For this reason, convective terms, corresponding to translational effects, are dropped from the equations. The Lagrangian step calculates the mass flow through the cell boundaries at time $t^n + \Delta t$. It is assumed throughout that the mass of the large particle is in motion only owing to the velocity component normal to the boundary. The final step determines the final fields of the Eulerian flow parameters at the time $t^{n+1} = t^n + \Delta t$. The equations of this step are the conservation laws of mass, momentum, and total energy, relating to a given cell (large particle) in finite difference form. The conservativity and total divergency of the difference scheme (divergent–conservative scheme) are guaranteed by the equation for total energy. In the final step (when a discrete model of the medium is being used), an additional calculation of density should be carried out. This smooths out fluctuations and increases the accuracy of the computations. Combining the steps, one obtains a series of difference schemes; this series, which constitutes the large-particle method, may be used for a broad range of numerical experiments.

The large-particle method may be interpreted from various points of view: the splitting method, the mixed Euler–Lagrange method, computation in local Lagrangian coordinates (Eulerian step) with scaling on the previous grid (Lagrangian and final steps), the difference notation for conservation laws for a fluid element (large particle), and the Eulerian difference scheme. The boundary conditions are formulated by introducing a series of fictitious cells (so that every computation point becomes an interior point and the same algorithm is maintained for all cells). One layer is sufficient for the first-order approximation scheme, two layers are sufficient for the second order, etc. The difference schemes of the large-particle method have been investigated (with regard to approximations, viscosity effects, stability) with the help of differential approximations.[14]

Application of explicit schemes of this method is ineffective in the case under consideration because the Mach number values ($M < 0.3$) are insignificant and the end-face clearance cross-sectional area changes are sizable ($F(\xi, t)/t \gg 1.0$). Both marked factors reduce the numerical calculation stability. (The Courant number permissible value, which is accepted in calculations, does not exceed $Co \leq 0.2 \div 0.4$.) The analysis establishes that the increase in stability of the numerical calculations up to $Co \approx 1$ and at small velocities ($M < 0.1$) can be achieved by modification of the large-particle method Euler stage finite difference schemes.[4,8] The stability of the numerical calculations may also be increased by using the differential approximation analysis method.[14]

Equations (16) and (17) for the definition of incident radiation density are solved by the sweep method.[15] The numerical solution of all other equations of the system is not difficult. In particular, it is possible to integrate Eq. (18) by using any known method, such as the Euler method.[15]

Stability and Convergence of the Numerical Algorithms

For the constructed numerical algorithms, autonomous and complex investigations of stability and convergence were conducted. The analysis of the stability of the finite difference scheme at time step Δt was executed by variation of the Courant number Co. The time step was determined from Courant–Friedrichs–Levy's stability condition:

$$\Delta t = Co \cdot \Delta\xi/(/U/ + C)_{\max} \tag{25}$$

The calculations were executed on a computational grid of 40 cells, at various Courant numbers, which were varied from 0.1 up to 0.95. In this case, the calculation results did not depend on the Courant number.

For the analysis of the convergence and accuracy of the numerical schemes, a number of test calculations for finite difference grids of various sizes (30, 40, 50, 60, and 80 cells) were executed. The deviations in computed values of CP velocity and pressure did not exceed 0.1 and 0.3%, respectively. Deviation in the computed values of the solid propellant charge surface ignition delay time did not exceed 1.2%.

The main calculations were executed on a computational grid with 40 cells.

Comparison with Fire Stand Test Data

To validate the mathematical model of the physicochemical processes, the numerical calculation results were compared with the fire stand test (FST) results. A pressure gauge was installed in the engine head end, namely, in the IS flange plug (denoted 1 and 5 in Fig. 1). Figures 4 and 5 show comparisons of the numerical calculation results (curves 1 and 2, continuous lines) with the FST results for the full-scale SPRM (curve 3, dotted line). Figure 4 shows CP pressure without boot break off, and Fig. 5 shows CP pressure with boot break off. In Fig. 4, curves 1 and 2 are the calculated CP pressure on the boundary between the front-end face clearance and the boot and in the SPRM front volume, and curve 3 is the experimentally measured CP pressure in the SPRM front volume. In Fig. 5, curves 1 and 2 are the calculated CP pressures on the boundary between the front-end face clearance and reopened cavity and in the SPRM front volume. For the calculations, the volume of the opened cavity was assumed to be $W_0^{\text{calc}} \approx 0.13$ m^3. Thus, the calculated boot break-off pressure was found to be $P_*^{\text{calc}} \approx 3.225$ MPa, and the experimentally determined boot break-off pressure was $P_*^{\text{exp}} \approx 3.153$ MPa. Curve 3 shows the experimental CP pressure in the SPRM front volume.

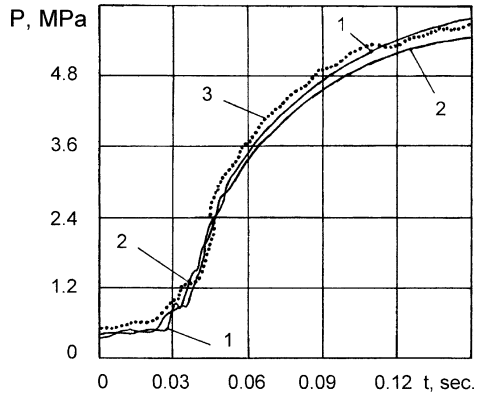

Fig. 4 CP pressure on the boundary between the front-end-face clearance and the boot and in the SPRM front volume without boot break off. Comparison of —— (1 and 2), numerical calculation results with .... (3), FST results for the full-scale SPRM front-end volume.

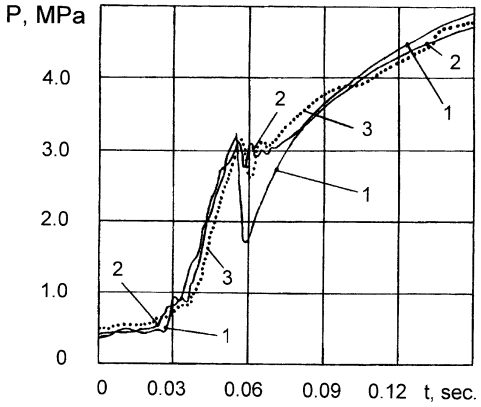

Fig. 5 CP pressures on the boundary between the front-end-face clearance and reopened cavity and in the SPRM front volume with boot break off. Comparison of —— (1 and 2), numerical calculation results with .... (3), FST results for the full-scale SPRM.

Simulation Results and Discussion

Tables 1 and 2 list the initial data used in the computer model. The IS charge is manufactured as a set of granulated elements, having a spherical form and pressed from the pyrotechnic mixture. The pyrotechnic mixture has the following chemical composition: technical barium nitrate 60%, titanium powder 35%, binding solution containing Mg compounds and graphite 5%.

The numerical research has shown that the transient processes caused by boot break off pose the greatest danger to the SPRM at the instant of boot break off. Therefore, the analysis of the anomalous processes was performed only for the instant of boot break off. The basic results of the numerical investigation of transient physicochemical processes after boot break off are shown in Figs. 4–13.

Table 1 Characteristics of the pyrotechnic ignition system

Parameter	Value
Propellant charge (pyrotechnic mixture)	
$T_{\text{ig}}^{\text{IS}}$, K	1090
$T_{\text{CP}}^{\text{IS}}$, K	3500
k^{IS}	1.276
γ_c^{IS}	0.62
ω_{IS}, kg	2.5
ρ_c^{IS}, kg/m^3	2930
u_1^{IS}, m/s	0.020
ν_c^{IS}	0.37
H^{IS}, m^2/s^2	4.44×10^6
Chamber	
L_{IS}, m	0.24
W^{IS}, m^2	0.003
$F_{\text{op}}^{\text{IS}}$, m^2	0.0127

Table 2 Characteristics of the solid propellant rocket motor

Parameter	Value
Propellant charge (composite)	
L_{PC}, m	2.0
D_{PC}, m	1.8
S_{PC}, m^2	7.0
ρ_c, kg/m^3	1850
u_1, m/s	0.00541
ν_c	0.23
H, m^2/s^2	6.54×10^6
Combustion chamber	
F_{CC}, m^2	0.0597
P_{D}, MPa	1.5

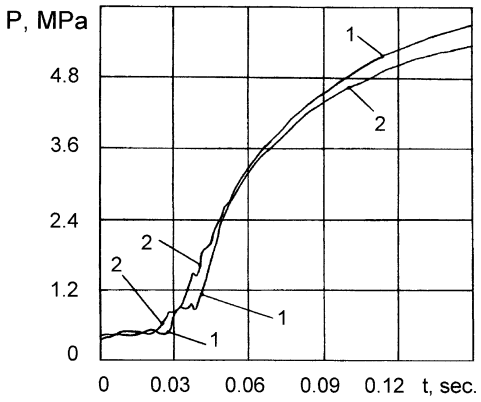

Fig. 6 Calculated CP pressure vs time for boot break off at $P_*^{\text{calc}} \approx$ 1.0 MPa.

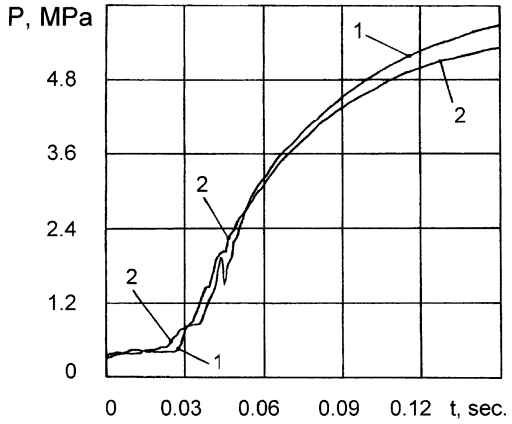

Fig. 7 Calculated CP pressure vs time for boot break off at $P_*^{calc} \approx$ 2.0 MPa.

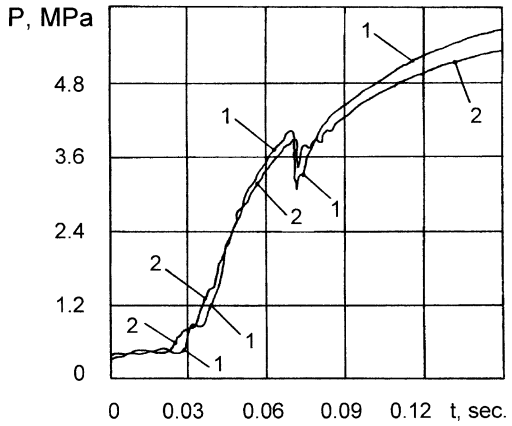

Fig. 8 Calculated CP pressure vs time for boot break off, at $P_*^{calc} \approx$ 4.0 MPa.

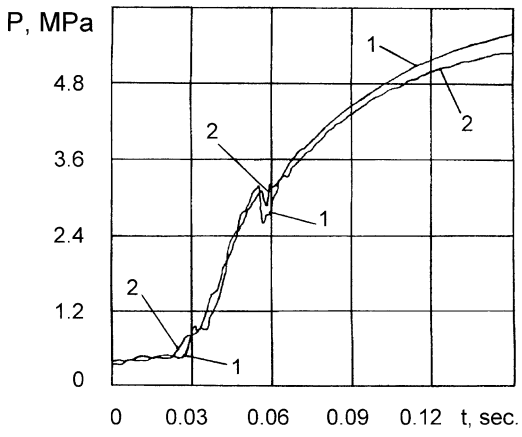

Fig. 9 Calculated CP pressure vs process time for case with boot break off at $P_*^{calc} \approx 3.175$ MPa and $W_0^{calc} \approx 0.03$ m^3.

The numerical investigations were executed taking into account the influence of a number of factors: the boot break-off pressure value, the cavity volume that opened after break off, the length over which the seal separates, and the duration in time of break off.

Figures 6–8 show calculated CP pressure vs time for break-off pressure values of $P_*^{calc} \approx 1.0$ MPa (Fig. 6), $P_*^{calc} \approx 2.0$ MPa (Fig. 7), and $P_*^{calc} \approx 4.0$ MPa (Fig. 8) with an opened cavity volume value equal to $W_0^{calc} \approx 0.06$ m^3. In Figs. 6–8, curves 1 and 2 correspond to the CP pressures on the boundary between the front end-face clearance and the reopened cavity and in the SPRM front volume, respectively. The analysis of the results shows that a marked influence on the CP pressure level in the vicinity of boot break-off is

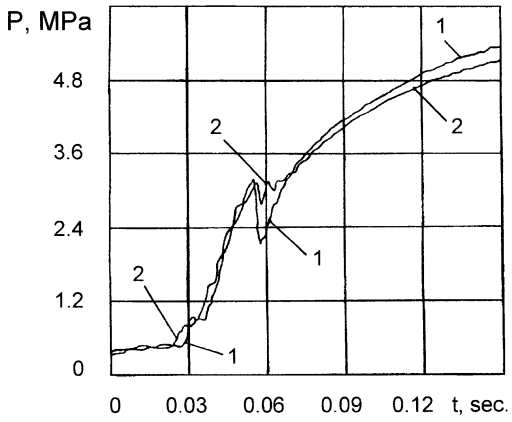

Fig. 10 Calculated CP pressure vs process time for case with boot break off at $P_*^{calc} \approx 3.175$ MPa and $W_0^{calc} \approx 0.06$ m^3.

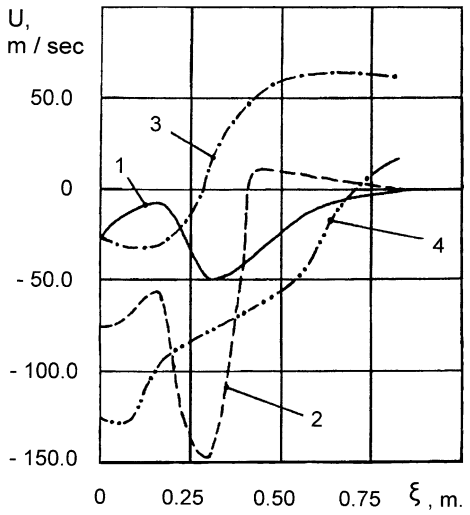

Fig. 11 Variations in CP flow velocity along the front-end-face clearance length: $W_0^{calc} \approx 0.03$ m^3, $t = 0.050$ s, $t = 0.057$ s, $t = 0.060$ s, and $t = 0.080$ s.

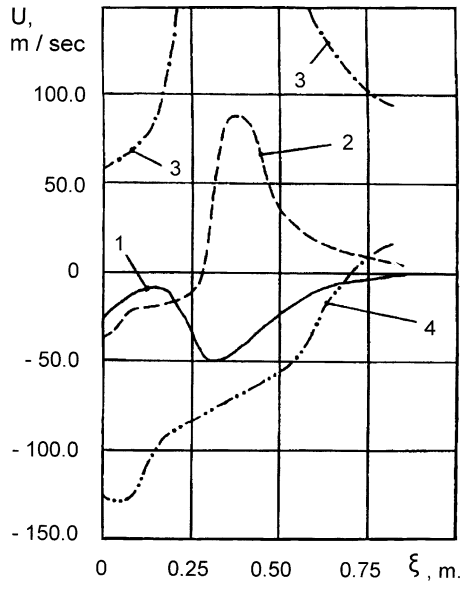

Fig. 12 Variations in CP flow velocity along the front-end-face clearance length: $W_0^{calc} \approx 0.06$ m^3, $t = 0.050$ s, $t = 0.057$ s, $t = 0.060$ s, and $t = 0.080$ s.

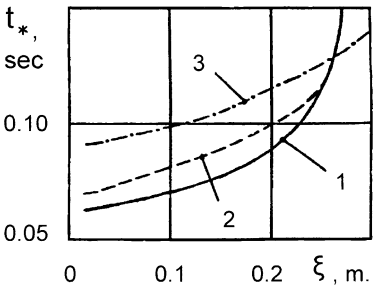

Fig. 13 Ignition delay time for propellant surface in reopened end-face cavity vs longitudinal coordinate for cases with boot break off: curve 1, $P_* = 3$ MPa, $L = 0.35$ m, and $W_0 = 0.03$ m^3; curve 2, $P_* = 4$ MPa, $L = 0.35$ m, and $W_0 = 0.03$ m^3, and curve 3, $P_* = 3$ MPa, $L = 0.46$ m, and $W_0 = 0.04$ m^3.

observed in cases when $P_*^{\text{calc}} > 2.0$ MPa. Thus, at $P_*^{\text{calc}} \approx 4.0$MPa (Fig. 8), the CP pressure drop (curve 1) is greater than 30%. The pressure decrease duration is 0.005–0.01 s, and its rate reaches $dP/dt = 20$ MPa/s. At the same time, the calculations show that the change in CP pressure caused by boot break off is less distinct on the boundary between the end-face clearance and the front volume (Figs. 6–8, curve 2). The pressure drop in these cases does not surpass 0.05–0.5 MPa.

The volume of the cavity opened by boot break off influences to a greater degree the transitional processes in the vicinity of the boundary between the end-face clearance and the separating boot. An analysis of this influence is presented in Figs. 5, 9, and 10. In Figs. 5, 9, and 10, the dependence of calculated CP pressure on process time is presented for cases in which boot break off occurs at $P_*^{\text{calc}} \approx 3.175$ MPa ($P_*^{\text{calc}} \approx 3.225$ MPa in Fig. 5), and the opened cavity volume is equal to $W_0^{\text{calc}} \approx 0.03$ m^3 (Fig. 9), $W_0^{\text{calc}} \approx 0.06$ m^3 (Fig. 10), and $W_0^{\text{calc}} \approx 0.13$ m^3 (Fig. 5). Again, curves 1 and 2 correspond to CP pressures on the boundary between the front end-face clearance and the reopened cavity and in the SPRM front volume, respectively.

The calculations show that at $W_0^{\text{calc}} > 0.04$ m^3 the transitional process develops abnormally. The pressure drop caused by boot break off is considerable (> 1.2 MPa) because the filling of the cavity occurs in the powerful compression wave mode (or in the shock wave mode). The danger of this type of transitional process development lies in that the powerful rarefaction wave will propagate along the end-face clearance toward the charge central channel and may cause either the extinction of the propellant charge or transition to an unsteady burning mode (chuffing of the engine). Another danger lies in that a compression wave propagating toward the newly opened cavity can produce dangerously large pressures in the vicinity of the upper boundary of the cavity, resulting in charge destruction.

Figures 11 and 12 present variations in CP flow velocity along the front end-face clearance length, during the propagation of a strong rarefaction wave at the opened cavity with a volume of $W_0^{\text{calc}} \approx 0.03$ m^3 (Fig. 11) and $W_0^{\text{calc}} \approx 0.06$ m^3 (Fig. 12). Curve 1 corresponds to time $t = 0.050$ s (before the beginning of the transitional period). Curve 2 corresponds to time $t = 0.057$ s, curve 3 to t = 0.060 s, and curve 4 to $t = 0.080$ s (completion of the transitional period). The CP velocity dependencies at $t = 0.050$ s are identical in Figs. 11 and 12, as are those at $t = 0.080$ s (curves 1 and 4). For the purposes of representation, it is assumed that the positive CP velocity value corresponds to the direction from the engine axis toward the nonflowing end-face clearance boundary.

As follows from Figs. 11 and 12, the intensity of the wave processes in the end-face cavity is much higher at $W_0^{\text{calc}} \approx 0.06$ m^3. For $W_0^{\text{calc}} \approx 0.03$ m^3, the maximum value of the CP velocity in the uncovered end face cavity is 63 m/s (Fig. 11, curve 3), whereas for $W_0^{\text{calc}} \approx 0.06$ m^3 the peak velocity is 486 m/s (Fig. 12, curve 3, peak not shown). The transient in the end-face clearance (in terms of CP velocity values) lasts between 0.02 s (for $W_0^{\text{calc}} \approx 0.03$ m^3) and 0.04 s (for $W_0^{\text{calc}} \approx 0.06$ m^3). The character of the dependence $U(t)$ becomes clearer if the dependence of the front end-face clearance cross-sectional area in the vicinity of the engine head end from the longitudinal coordinate (Fig. 2) is taken into account.

The intensive compression wave results in an increase of the CP pressure maximum level in the nonflowing boundary area. The calculations reveal that at $W_0 = 0.04$ m^3 the maximum pressure values correspond to $P_{\max} \approx 8.0$ MPa.

The calculations also show that the propellant surface ignition delay time in the reopened end-face cavity is increased with an increase in P_* and in L (Fig. 13). Curve 1 shows the case with $P_* = 3$ MPa, end-face cavity length $L = 0.35$ m, and $W_0 = 0.03$ m^3. Curve 2 shows the case for $P_* = 4$ MPa, end-face cavity length $L = 0.35$ m, and $W_0 = 0.03$ m^3. Curve 3 shows the case for $P_* = 3$ MPa, length $L = 0.46$ m, and $W_0 = 0.04$ m^3. The flame propagation velocity on the propellant surface is more or less identical for all three cases.

Development of Anomalous Mode Ignition in Technical Applications

The occurrence of anomalous mode ignition in the large-sized solid propellant boosters of the reusable transport space system (RTSS) is extremely undesirable. The asymmetry of the two solid propellant boosters in the RTSS structure puts strict limits on the level of instability permissable during ignition processes and subsequent combustion in the boosters' combustion chambers. Realization of the earlier described anomalous mode ignition in one of the boosters can lead to infringement of the symmetry of the RTSS total thrust distribution and appearance of a destabilizing moment. It may also, depending on the influence of the thrust misalignment on the RTSS trajectory, have unexpected effects on the payload and even lead to loss of control of the RTSS.

The appearance of the earlier described anomalous ignition mode, which is accompanied by intensive shock waves in the engine combustion chamber, is no less dangerous for modern submarine-launched ballistic rockets.[16] The design of these rockets is characterized by the use of every available part of the volume of the envelope of the rocket case. The inception of unpredictable vibrational and impact loads in the engine chamber can trigger anomalous resonant effects in the whole system and result in damage to its various units and elements, such as the gyros in the control system.

Technology for the Prevention of Anomalous Ignition Processes

Nevertheless, the calculations and FST described here demonstrate that for safe ignition of the case-bonded solid propellant charge burning surface in the narrow front-end-face clearance (stagnation zone), it is necessary to provide CP flow supply from the IS into the stagnation zone, as the cross-section of the stagnation zone increases. The appearance of abnormal ignition modes in the SPRM can, thus, be prevented.

On the basis of the results of numerical analysis of the physicochemical processes during operation of traditional ignition systems in the high-loading-density SPRM (Fig. 1), the appropriate technology for prevention of anomalous ignition of the solid propellant charge was developed. This technology provides uniformity of SPRM operation during the ignition-transient period by means of the CP selection, coming from the IS, both in space orientation and in time.

For practical realization of the new ignition technology, a special SPRM IS design scheme was developed. In Fig. 14 the longitudinal

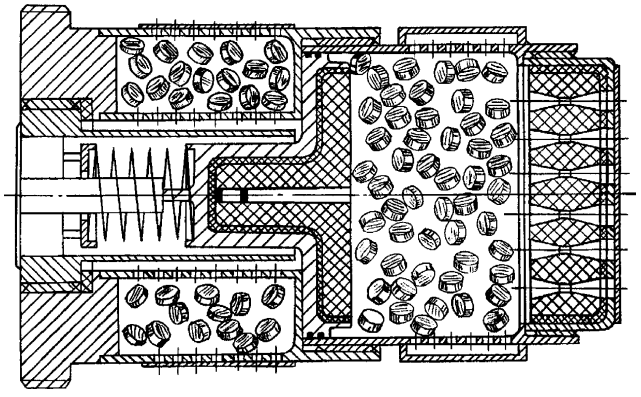

Fig. 14 Large SPRM pyrotechnic ignition system that provides gradual CP flows in large SPRM combustion chamber in the longitudinal and crosswise directions.

cross section of the newly developed pyrotechnic IS design is shown schematically. The pyrotechnic IS (Fig. 14) consists of the cylindrical casing, divided into two sections, and the flange plug. The main section (on the right) contains the main pyrotechnic ignition charge, and the additional section (on the left) contains the additional pyrotechnic ignition charge. On the right end of the main section is the accelerating section. A spring-loaded mobile piston with an initiating device is installed in the cavity of the main section. The IS casing surface is covered by a thermal insulating layer. When the IS is installed in the engine, the perforations on the lateral surface of the additional section are placed opposite the cavity of the nonflowing front-end-face clearance.

The charges installed in the accelerating section and in the casing of the mobile piston are manufactured from an exothermic hydrogen-generating mixture (EHM). As the EHM is used the mechanical mixture of powders of the solid fuel, carbide or nitrite-forming metals of Mendelyeev's periodic system groups 4–5 and the solid oxidizer, hydrogen-containing compounds of carbon or nitrogen. The combustion processes of the mentioned charges represents the self-propagating high-temperature synthesis.

The mobile piston provides the required delay in ignition of the additional pyrotechnic charge. Movement of the piston is initiated as the main ignition charge is burning out. When the piston is displaced into the perforation zone on the lateral surface of the main section, the CP of the main ignition charge start to flow into the space behind the piston and ignite the additional ignition charge. This provides a time-delayed CP flow supply from the IS in the crosswise direction, into the engine front-end-face clearance.

The charges installed in the accelerating section and in the casing of the mobile piston are highly effective absorbers of the CP acoustic oscillation energy. Therefore, the IS design described here provides suppression of the unstable combustion modes and absorption of the main ignition charge CP acoustic oscillation energy in a wide frequency band in the IS main section cavity. The accelerating section provides additional acceleration of the CP flowing out from the IS main section. At the same time, the charges installed in the accelerating section and in the casing of the mobile piston function as atomic hydrogen generators. On the SPRM charge surfaces, the atomic hydrogen recombines in the diatomic structure, frees the dissociation energy, and transmits this energy to the propellant surface. This provides an improved heat supply to the SPRM charge surfaces: the hydrogen heat conduction practically an order higher than the IS charges CP heat conduction, and hydrogen viscosity approximately two times lower than at the IS charges CP.

Figure 15 shows the operational stages of the pyrotechnic IS described here in the high-loading-density SPRM. As shown in Fig. 15, in stage 1, the CP flows from the IS main section 2 into the solid propellant charge channel 3 in the longitudinal direction. Joint elastic deformation will take place in both the propellant charge and the SPRM case. The end-face clearance cavities will be increased up to the necessary sizes before the moment of flame appearance on the propellant charge surface (stage 2). In stage 3, the CP flows from the IS additional section 1 into the front-end-face clearance in the cross wise direction, to improve SPRM ignition-transient period of operation. This will provide an improved heat supply to the propellant surface in the nonflowing front-end-face clearance. Under these conditions, the $\partial P/\partial t$ maximum values are reduced, the flame propagation velocity along the end-face clearance increases, the ignition delay time of the propellant surface located in the end-face cavity decreases, and the probability of boot break off is significantly reduced.

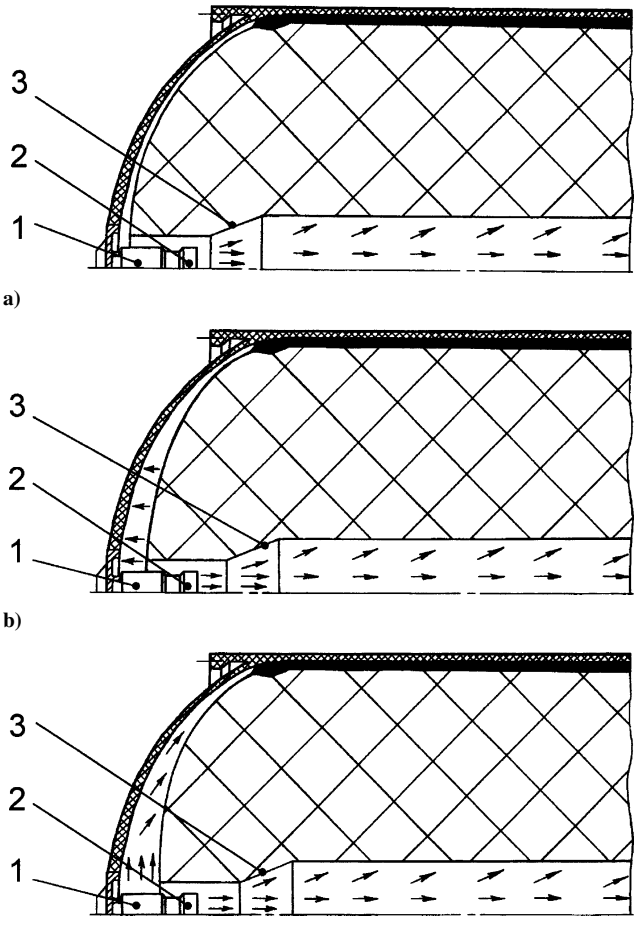

Fig. 15 Consecutive stages of the pyrotechnic ignition system operation in the high-loading-density SPRM: a) stage 1, b) stage 2, and c) stage 3.

Conclusions

The results of the research described here have confirmed that modern high-loading-density SPRM can be improved through investigation of technologies for optimal organization of the intrachamber processes during SPRM initial stage operation, with the purpose of reducing the impact and vibrational loads both on the SPRM design elements and on the various onboard systems.

The main factors that influence the process in the engine after boot break off are as follows: the boot break-off pressure, the cavity volume opened by break off, the length over which there is boot break off, and the duration in time of the boot break-off period. The nonstationary processes caused by boot break off are the most dangerous to the engine operation at the instant of break off.

On the basis of the numerical modeling results, new technology for the ignition of case-bonded solid propellant charges was developed. This technology allows reduction of the ignition-transient period time without a pressure increase in the engine combustion chamber and simultaneously reduction of the thermal loads on the charge and the structural elements of the engine combustion chamber. This technology also provides uniformity of the SPRM operation during the ignition-transient period by means of the selection of the CP exiting the IS, both in space and in time. For practical realization of the new ignition technology, a special SPRM IS design scheme was elaborated.

References

[1]Smirvov, N. N., "The Convective Combustion in the Channels and Cracks in the Solid Propellant," *Physics of Combustion and Explosion Journal*, Vol. 21, No. 5, 1985, pp. 29–36 (in Russian).

[2]Smirvov, N. N., and Dimitriyenko, I. D., "The Convective Combustion Mode in the Deformable Solid Propellant with the Longitudinal Channels," *Physics of Combustion and Explosion Journal*, Vol. 22, No. 3, 1986, pp. 59–67 (in Russian).

[3]Lipanov, A. M., Aliev, A. V., Bodnar, T. A., Druzhbin-Hodos, V. M., and Litvinov, L. A., "The Flame Propagation in the Narrow Non-flowing Deformable Channel," *Physics of Combustion and Explosion Journal*, Vol. 26, No. 3, 1990, pp. 27–33 (in Russian).

[4]Lipanov, A. M., Bobryshev, V. P., Aliev, A. V., Spiridonov, F. F., and Lisitsa, V. D., "Numerical Experiment in the Theory of the SPRM," Nauka, Ekatherinburg, Russia, 1994, p. 303 (in Russian).

[5]Price, E. W., "L* -Instability," *Nonsteady Burning and Combustion Stability of Solid Propellants*, Progress in Astronautics and Aeronautics, Vol. 143, AIAA, Washington, DC, 1992, Chap. 9, pp. 325–359.

[6]Kutateladze, S. S., "The Heat Transfer and Hydrodynamics Resistance: The Handbook," Energoatomizdat, Moscow, Russia, 1990, pp. 245–267 (in Russian).

[7]Viliyunov, V. N., "The Theory of the Condensed Materials Ignition," Nauka, Novosibirsk, Russia, 1984, pp. 148–167 (in Russian).

[8]Lipanov, A. M., Lukin, A. N., and Aliev A. V., "Numerical Simulation of the Nonstationary Spatial Gasdynamics Processes Accompanying the Pelletized Solid Propellant Combustion in a Gas Generator," *Challenges in Propellants and Combustion: 100 Years After Nobel*, edited by Kenneth K. Kuo, Begell House, New York, 1997, pp. 1164–1178.

[9]Shapiro, A. H., "The Dynamics and Thermodynamics of Compressible Fluid Flow," Vol. 1, Ronald, New York, 1953, pp. 61–67.

[10]Sorkin, R. Y., "The Theory of the Intrachamber Processes in the Solid Propellant Rocket Systems: Internal Ballistics," Nauka, Moscow, 1983, pp. 117–142 (in Russian).

[11]Davydov, Y. M., "Multi-Parameter Splitting Schemes for Solution of Spatially Three-Dimensional Non-Stationary Problems," *Reports of the USSR Academy of Sciences*, Vol. 247, No. 6, 1979, pp. 1346–1350 (in Russian); also *Soviet Mathematical Reports* (English translation, American Mathematical Society), Vol. 24, No. 8, 1979, pp. 229–236.

[12]Davydov, Y. M., "The Architectural Matrix of Approximate Viscosity," *Reports of the USSR Academy of Sciences*, Vol. 278, No. 4, 1984, pp. 789–796 (in Russian); also *Soviet Mathematical Reports* (English translation, American Mathematical Society), Vol. 30, No. 2, 1984, pp. 460–464.

[13]Davydov, Y. M., "Large Particles Method," *Encyclopaedia of Mathematics*, Vol. 5, Kluwer Academic, Dordrecht, The Netherlands, 1990, pp. 358–360.

[14]Davydov, Y. M., and Skotnicov, V. P., "The Large Particles Method: Problems of Approximation, the Schematic Viscosity and Stability," Computer Center of the USSR Academy of Sciences, Moscow, 1978, pp. 36–54 (in Russian).

[15]Samarskii, A. A., and Gulin, A. V., *Numerical Methods*, Nauka, Moscow, 1989, pp. 356–374 (in Russian).

[16]Velitchko, I. I. (ed.), *The Ballistic Rockets of the Submarines of Russia. The Selected Articles*, State Rockets Centre, "The Academician V. P. Makeev's Constructor Bureau," Miass, Russia, 1994, pp. 176–197 (in Russian).